Available online at www.sciencedirect.com
ScienceDirect
Trans. Nonferrous Met. Soc. China 35(2025) 1803−1821
Transactions of Nonferrous Metals Society of China
www.tnmsc.cn

Silicide precipitation behavior of Si-containing near-β titanium alloy and its effect on grain refinement

Peng-kun GUO[1], Chang-jiang ZHANG[1,2,3], Hong FENG[1],
Fu-yin HAN[1], Hang LI[1], Jian-chao HAN[3], Fan PENG[2], Peng CAO[4]

1. College of Materials Science and Engineering, Taiyuan University of Technology, Taiyuan 030024, China;
2. Kocel Machinery Co., Ltd., Yinchuan 750021, China;
3. Engineering Research Center of Advanced Metal Composites Forming Technology and Equipment, Ministry of Education, Taiyuan 030024, China;
4. Department of Chemical and Materials Engineering, University of Auckland, New Zealand

Received 11 October 2023; accepted 28 April 2024

Abstract: This study investigated the effect of Si addition on the microstructure and the silicide precipitation behavior in a novel near-β titanium alloy. The results show that coarse and continuous silicides were preferentially precipitated at the grain boundary during the solidification process, and the β grain size of the as-cast alloy was refined. Dynamic recrystallization occurs under isothermal compression, and the silicide could inhibit the growth of recrystallized grains. The element redistribution and dislocation accumulation during hot deformation promote the dynamic precipitation of silicide, resulting in a discontinuous distribution of silicides at the grain boundaries. This work provides insight into how silicide dynamic precipitation will affect the microstructure and plastic deformation behavior of metal alloys.
Key words: near-β titanium alloy; hot compression; silicide; grain refinement; dynamic precipitation

1 Introduction

Titanium (Ti) and titanium alloys are widely used in aerospace, military, biomedical, and other fields because of their high specific strength, corrosion resistance, and excellent biocompatibility, which are known as “light structural material,” “advanced functional material,” and “future metal” [1−4]. In particular, high-strength near-β titanium alloys have attracted much attention because of their high strength, good hardenability, and excellent workability [5,6]. However, high-strength near-β titanium alloys face the problem of coarse grains and poor mechanical properties of the as-cast alloys. In recent years, many attempts have been made to improve the microstructure and mechanical properties of high-strength near-β titanium alloys. Generally, these approaches can be categorized into two types: one obtained via specific processing techniques and the other through alloy composition modifications [7]. In processing technology, appropriate thermal-mechanical treatments, cold deformation processes, and heat treatment processes are often used [5,8,9]. In the realm of composition design, various innovative β titanium alloys have been continuously proposed and explored [10−12].

The stability of the β phase is often predicted by the molybdenum equivalent number ($[Mo]_{eq}$) [13]. LI et al [14] optimized the α+β microstructure and found a trade-off between strength and toughness

Corresponding author: Chang-jiang ZHANG, Tel/Fax: +86-351-6010022, E-mail: zhangchangjiang@tyut.edu.cn;
Hong FENG, Tel/Fax: +86-351-6010022, E-mail: fenghong@tyut.edu.cn
https://doi.org/10.1016/S1003-6326(25)66784-7

based on $[Mo]_{eq}$ and d-electron theory. And the strength increases by 12%, while the toughness only decreases by 4%. The $[Mo]_{eq}$ of β titanium alloy is not less than 8 [15]. Mo, Cr, and V are often added as β-stable elements in near-β and β titanium alloys [5]. By adding V to change the β phase content and α phase morphology, SUN et al [16] found that α/β interface dislocation slip activation could promote the discontinuous yield of titanium alloys during tensile at room temperature. As a neutral element, Zr has high solubility in both α and β titanium alloys. Adding Zr can reduce the solubility of Si in the matrix and promote silicide precipitation [17−19]. The addition of Si has a positive effect on grain refinement, and according to the growth-restriction factor (Q) theory, Si is the second only to O in terms of the growth-restriction effect [20]. SUN et al [21] studied the Ti−5Al−5Mo−5Cr−3Nb−2Zr alloy with Si addition. They found that the TiSi phase precipitated in the microstructure after solution aging, and the tensile strength of the alloy was improved when the Si content exceeded 0.2 wt.%.

In recent years, many studies have focused on high-temperature titanium alloys containing Si prepared by ingot metallurgy [22]. Still, there have been few studies on high-strength titanium alloys containing Si, especially those with high Si content. The reports on controlling silicide precipitation and precipitation mechanisms in high-strength titanium alloys are limited. It is well known that if the content of Si in β titanium alloy prepared by conventional ingot metallurgy processes exceeds 0.5 wt.%, the ductility will be significantly affected by the coarse eutectic $S2$ phase silicide precipitation at grain boundaries. However, some studies have shown that hot deformation and dislocation accumulation will accelerate the diffusion of elements, resulting in the redistribution of Zr and Si elements, thus promoting the dynamic precipitation of silicides [23−26]. Therefore, by tailoring the dynamic precipitation of silicide, the coarse and continuous silicide precipitated from the grain boundary of the β titanium alloy is expected to be broken. So, it is necessary to study the tailoring mechanism of silicides in high-strength near-β titanium alloys to solve the problem that high Si content β titanium alloy prepared by conventional ingot metallurgy processes precipitates coarse and continuous silicides at grain boundaries. In particular, the near-β titanium alloy modified with a high Si content for high performance is of great significance. At the same time, titanium, a metal with high-stacking fault energy, is prone to dynamic recovery (DRV) during hot deformation but not to dynamic recrystallization (DRX) [27]. Moreover, high-strength near-β titanium alloys are also sensitive to deformation temperature. Therefore, it is necessary to study the evolution of microstructures during hot deformation.

Based on the grain refinement effect of adding Si to titanium alloy, as well as a dearth of research into the silicide precipitation and tailoring mechanisms of high-strength near-β titanium alloy, the novel near-β titanium alloys with nominal composition Ti−4Al−7Mo−4V−3Cr−3Zr−xSi (x=0, 0.4, 0.8, 1.2, wt.%) were designed and prepared by ingot metallurgy in this study. The microstructure of the alloy, the formation of silicide precipitates during solidification, and the manipulation of silicide precipitation during hot deformation were studied. It provides insights into using silicides to enhance the properties of high-strength near-β titanium alloys.

2 Experimental

2.1 Materials and method

In this study, an alloy with a nominal composition of Ti−4Al−7Mo−4V−3Cr−3Zr (wt.%) was designed. The value of $[Mo]_{eq}$ is 10.48, suggesting the alloy is a near-β titanium alloy. The respective metal (Ti, Al, Cr, Zr) and intermediate alloy (Al−Mo, Al−V) ingots or blocks and single-crystalline silicon were charged in a vacuum induction furnace in a water-cooled copper crucible, as per the compositions of Ti−4Al−7Mo−4V−3Cr−3Zr−xSi (x=0, 0.4, 0.8, 1.2, wt.%). The ingots were melted at least three times to ensure uniform composition. Each button ingot had a mass of 50 g, and the compression samples were taken from the center of each button ingot.

The uniaxial hot compression tests were carried out at 850, 900, 950, and 1000 °C on a Gleeble−3800 thermal simulation test machine. The test specimen size was d8 mm × 12 mm. The samples were heated at a ramp rate of 5 °C/s and held for 5 min before the test. The height reduction during compression was 70%, and the strain rate was 0.01 s^{-1}. The temperature was measured with a

thermocouple inserted at the mid-span of the sample. After the compression test, the deformed samples were immediately quenched in water to maintain the deformation microstructure.

2.2 Characterization of microstructure and properties

The specimen for optical microscopic (OM) observations was mechanically ground with 80 to 2000 grit SiC papers, followed by electro-polishing. The electro-polishing solution contained perchloric acid, *n*-butyl alcohol, and methanol, with a volume ratio of 1:3:6. After polishing, the surface of the specimen was etched with Kroll's reagent. The observed surface of the hot compression specimen was the central region parallel to the compression direction. The optical microstructure was characterized by a DM4M Leica OM. The Zeiss Geimini−300 scanning electron microscope (SEM) with an energy dispersive spectrometer (EDS) was used to characterize the SEM microstructure. The JEOL-JSM-IT500 field emission environmental SEM with an electron backscattered diffraction (EBSD) system was used for the EBSD characterization. The EBSD analysis was performed on the electro-polished cross sections. The EBSD characterization step size was 2 μm. The average equivalent diameter was calculated using Image-Pro Plus software. The FEI Tecnai F20 transmission electron microscope (TEM) was used for the TEM analysis. The TEM specimen with a diameter of 3 mm was cut from the central area of the compressed specimen parallel to the compression direction, and the thickness was mechanically ground to 40 μm, followed by ion-beam thinning. Phase analysis was carried out using Empyrean X-ray diffraction (XRD). The diffraction angle (2θ) changed from 30° to 80° with a scanning step of 0.02°.

The room-temperature compression experiments were conducted on an Instron−5969 electronic universal material testing machine. The specimen size was d4 mm × 6 mm, and the crosshead speed was 0.5 mm/min. Each sample was tested three times. The Vickers hardness tester HVS−1000A was used to test the Vickers hardness of the material with a load of 4.9 N for 15 s. Six readings from various locations were taken, and the average value of these 6 readings was reported as hardness.

3 Results

3.1 Microstructure of as-cast alloys with different Si contents

Figure 1 shows the XRD patterns of the as-cast alloy, presenting a single β-Ti phase in all the samples. Due to the small size or low quantity, silicide phases were not observed in XRD. Nevertheless, the magnified XRD pattern shows that the $(110)_{\beta\text{-Ti}}$ peak shifts to a higher angle due to the addition of Si. The dissolved Si atoms are known to reduce interplanar spacing, resulting in the distortion of the β phase lattice [28].

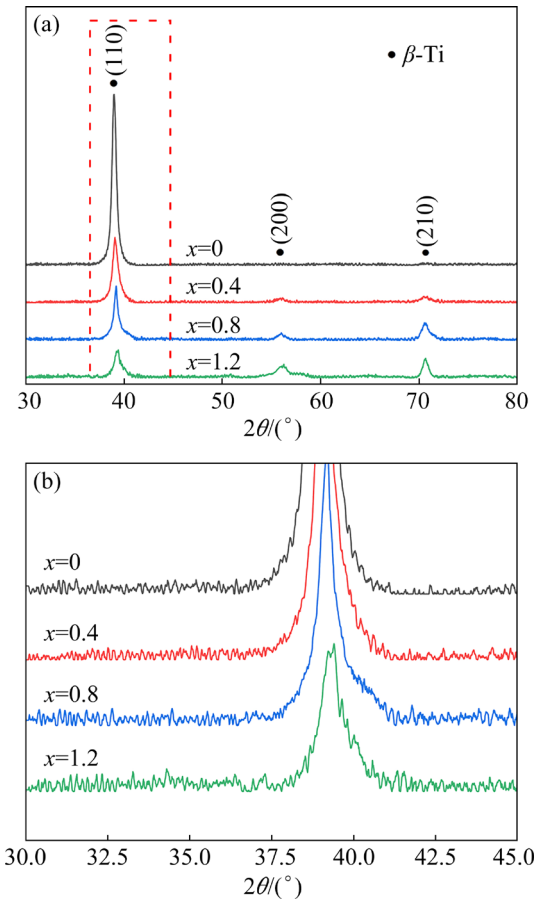

Fig. 1 XRD patterns of as-cast Ti−4Al−7Mo−4V−3Cr−3Zr−xSi alloys (a) and magnified patterns (b) for area marked in (a)

Figure 2 shows the SEM−EDS results of as-cast alloys with different Si contents, and OM images are shown in the lower left corner of the SEM images. As can be seen from the SEM images in Figs. 2(b) and (e), the alloy has no silicide precipitation with 0.4 wt.% Si. However, when 0.8 wt.% Si is added to the as-cast alloy, coarse and

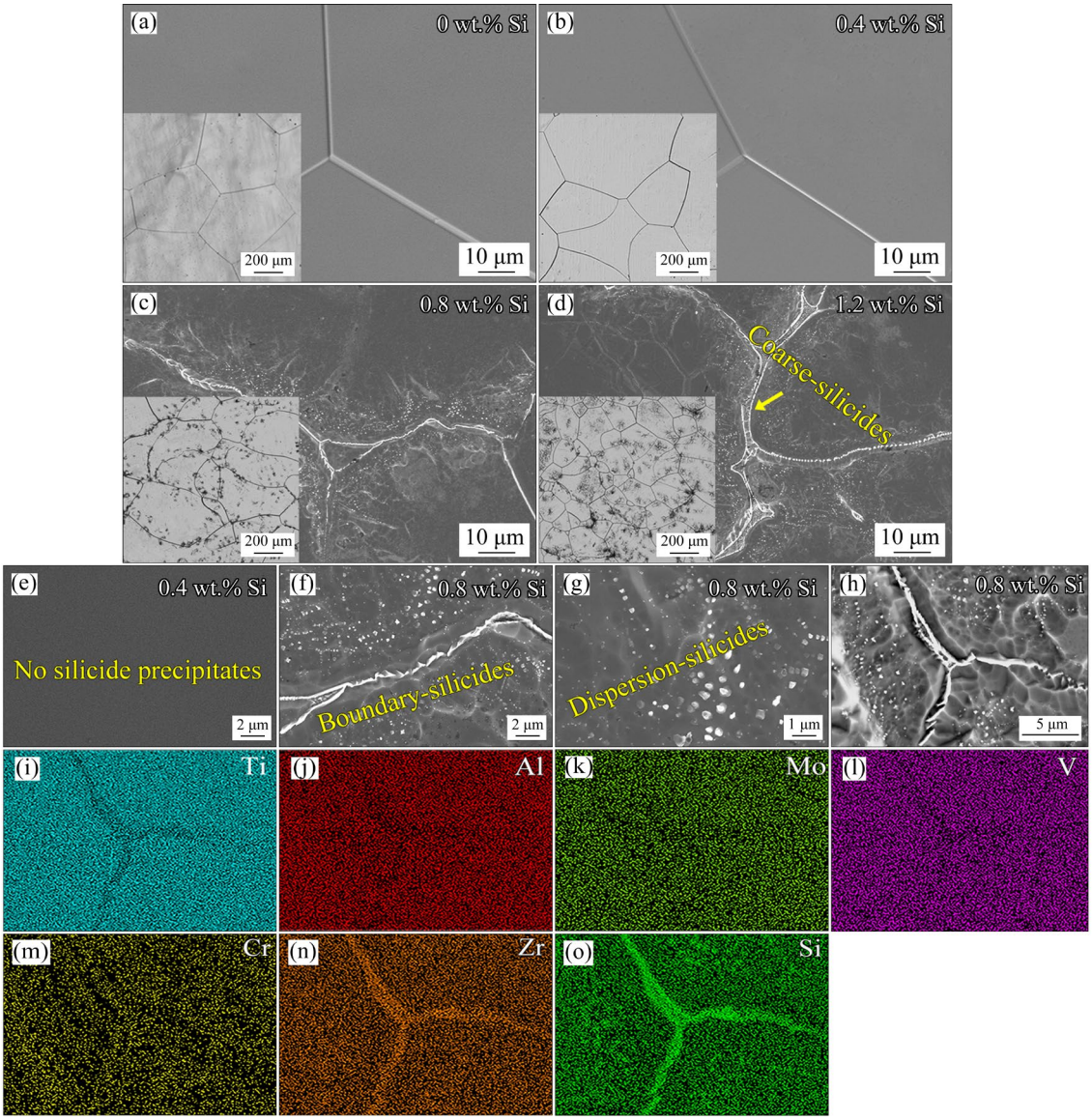

Fig. 2 SEM images of as-cast alloy with different Si contents (a−d), high-magnification SEM images (e−g), and EDS mappings of as-cast alloy with 0.8 wt.% Si (h−o)

continuous silicides are distributed at the grain boundaries, and fine dot-shaped silicides are distributed in the grain interior (Figs. 2(c), (f), and (g)). However, the distribution of silicides in the grain interior is heterogeneous and gathers near the grain boundary. It can be seen from Fig. 2(d) that more silicides precipitate, and the silicides are thicker at the grain boundaries when 1.2 wt.% Si is added to the as-cast alloy. Figures 2(h−o) show the EDS results of the 0.8 wt.% alloy. It can be seen that Si and Zr elements are enriched in the precipitates, which proves that the precipitates are silicides containing Ti, Zr, and Si. In addition, it can be seen from the OM images that the β grain size decreases with the increase in Si content. The average β grain size of Ti−4Al−7Mo−4V−3Cr−3Zr alloy was about 513.17 μm. When 0.4 wt.% Si, 0.8 wt.% Si, and 1.2 wt.% Si were added, the average β grain size was about 406.91, 230.37, and 141.86 μm, respectively. This is due to the growth-restriction effect of Si addition [29].

3.2 Hot deformation behavior

It is well known that the precipitation of coarse and continuous silicides at grain boundaries will reduce the ductility of materials. Considering the precipitation and distribution of silicides in as-cast alloys, it is necessary to study the hot deformation behavior of the alloys. We selected 0.4 wt.% Si and 0.8 wt.% Si alloys for the hot compression test

to analyze the microstructure evolution, silicide precipitation, and distribution under hot deformation, respectively. Figure 3 shows the true stress−strain curves of the as-cast alloys with 0.4 wt.% Si and 0.8 wt.% Si addition under hot compression at different temperatures, respectively. It can be seen that the peak stress of the material is higher under hot compression at 850 °C, mainly because the material has high deformation resistance at low temperatures and high dislocation density. Beyond the yield point, the sample experiences a competing softening and hardening phenomenon, finally reaching a dynamic equilibrium (a long strain plateau). When the deformation temperature increases, the process of reaching dynamic equilibrium will be accelerated. This is because as the temperature increases, the deformation resistance of the material decreases, the dislocation density generated by deformation decreases, and the work hardening rate decreases, so the small deformation amount makes it easy to achieve dynamic equilibrium [30,31].

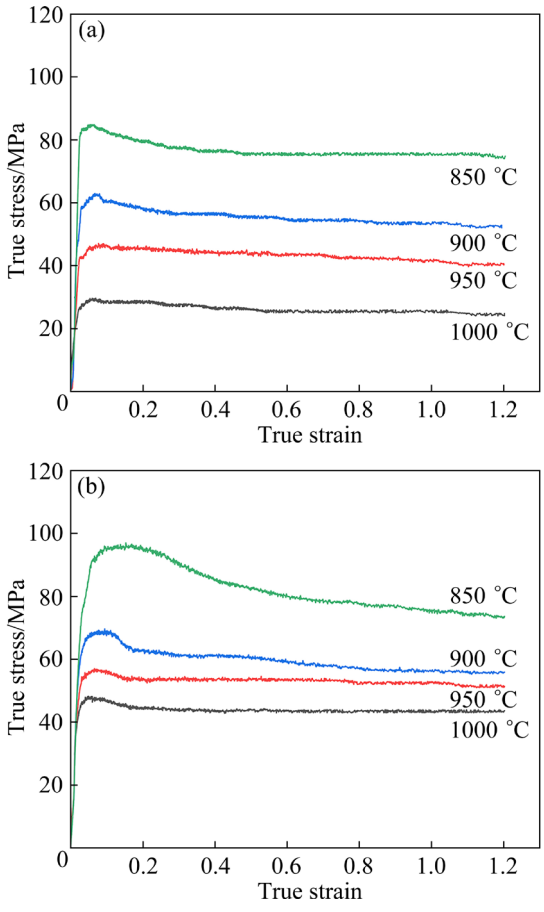

Fig. 3 True stress−strain curves under hot compression at different temperatures: (a) 0.4 wt.% Si alloy; (b) 0.8 wt.% Si alloy

The hardening of the material deformation process is mainly due to the increased dislocation density, and the existence of the precipitated phase in the microstructure will also hinder the dislocation movement and increase the deformation energy. The softening effect is due to deformation heat, DRV, and DRX, which cause the dislocations to rearrange and annihilate [30]. The higher the hot compression deformation temperature, the lower the peak stress, the shorter the dynamic softening interval, and the larger the dynamic equilibrium interval. In addition, the flow stress of the 0.4 wt.% Si alloy is lower than that of the 0.8 wt.% Si alloy because of the strengthening effect of Si and the higher volume fraction of silicide in the microstructure, which increases the strength and the deformation resistance.

Figure 4 shows the OM images of the as-cast alloys with 0.4 wt.% Si and 0.8 wt.% Si added under hot compression at different temperatures, respectively. It can be seen from Fig. 4(a) that for the 0.4 wt.% Si alloy under hot compression deformation at 850 °C, β grains are elongated perpendicular to the compression direction, and some silicides are precipitated, but the distribution of silicides is heterogeneous. The upper right corner of Fig. 4(a) is the OM image of the 0.4 wt.% Si as-cast alloy after heating to 850 °C for heat preservation and then water quenching without deformation. The comparison of the microstructure before and after deformation shows that most of the silicides observed after hot compression at 850 °C should be precipitated in the process of the hot compression deformation. The diffusion, redistribution, and segregation of Si elements are caused by high-temperature deformation and accumulated dislocation, which promote the dynamic precipitation of some silicides [23]. For the 0.8 wt.% Si alloy, after 850 °C hot compression deformation, more silicides are dispersed in the grain interior (Fig. 4(e)).

In addition, with the increase in deformation temperature, the number of silicides precipitated decreases due to the high solubility of Si at high temperatures. At the same time, the high deformation temperature promotes DRX. It can be observed from Fig. 4(c) that there are obvious DRX grains under hot compression deformation at 950 °C. This is due to the increased recrystallization nucleation and growth rate when the temperature

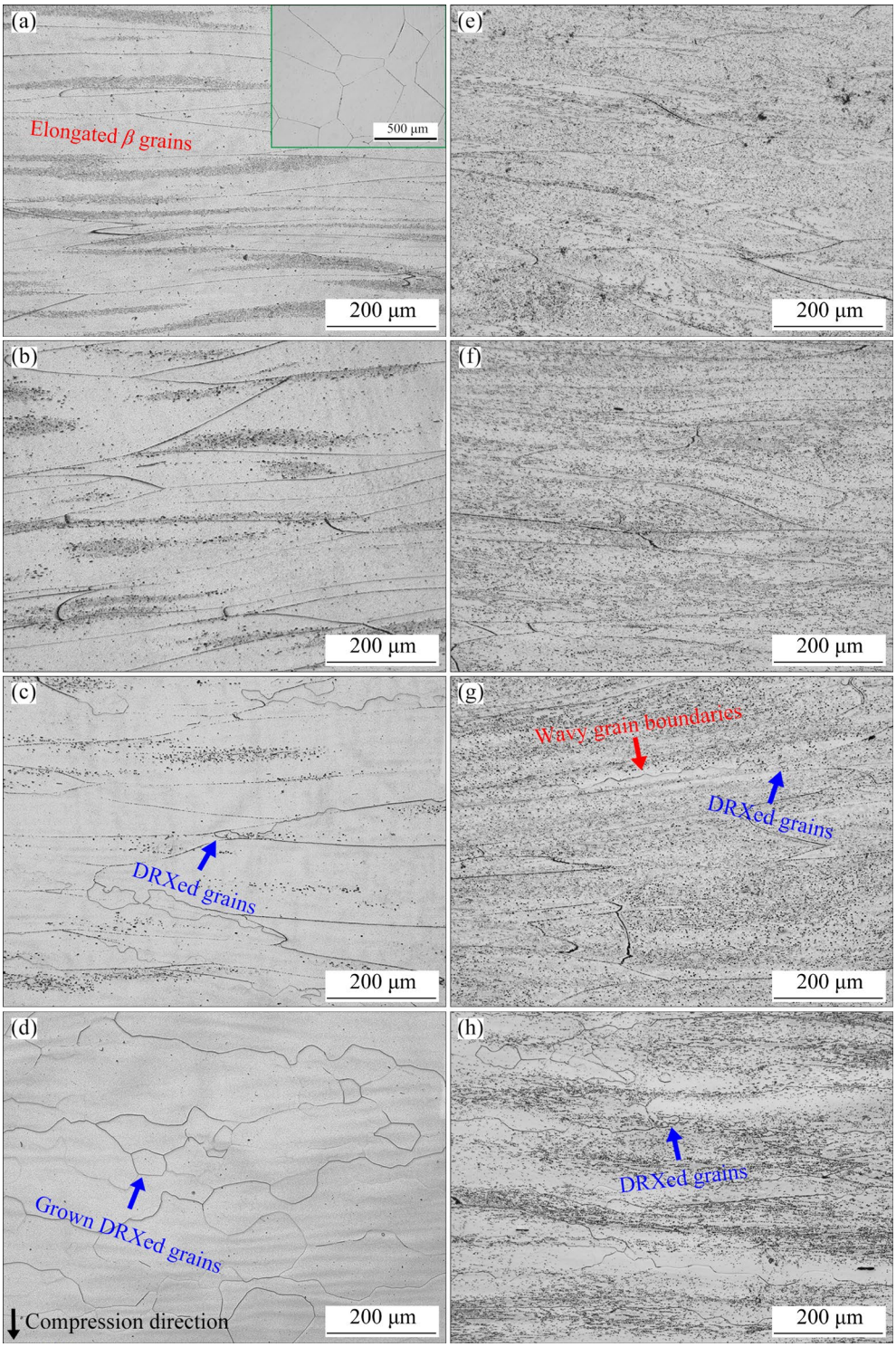

Fig. 4 OM images under hot compression at 850 °C (a, e), 900 °C (b, f), 950 °C (c, g), and 1000 °C (d, h): (a−d) 0.4 wt.% Si alloy; (e−h) 0.8 wt.% Si alloy

rises [30]. The recrystallized grains of the 0.4 wt.% Si alloy grow significantly under 1000 °C hot compression deformation, and the silicide is no longer visible under the OM image (Fig. 4(d)). It can be seen from Fig. 4(g) that in the 0.8 wt.% Si alloy after hot compression deformation at 950 °C, some wavy β grain boundaries appear and some DRX grains form. The 0.8 wt.% Si alloy after 1000 °C hot compression deformation shows obvious DRXed grains, the quantity of silicides is significantly reduced, and the distribution is heterogeneous (Fig. 4(h)). In addition, compared

with the 0.4 wt.% Si alloy, the recrystallized grain size of the 0.8 wt.% Si alloy is smaller because silicides inhibit the growth of DRX grains by hindering grain boundary migration.

Figure 5 shows the SEM images of 0.4 wt.% Si alloy under hot compression at different temperatures. It can be seen from Fig. 5(a) that after hot compression deformation at 850 °C, dot-shaped silicides are distributed at the grain boundaries and within the grain interior. The size of silicides at the grain boundaries is larger than that within the grain because Si is easy to enrich at the grain boundary, and silicide is preferentially precipitated at the grain boundary and grows up [24]. It can be seen from the SEM images that with the increase in deformation temperature, the size of the silicide increases and the quantity decreases. This is because the dislocation density in the deformed microstructure is low at high temperatures, which leads to a decrease in the nucleation site of silicides [22]. However, as the deformation temperature increases, the increased size of silicides may be due to their coalescence and growth at high temperatures. It can be seen from Fig. 5(d) that after hot compression deformation at 1000 °C, dot-shaped silicides are distributed at the grain boundaries, while almost no silicides are precipitated in the grain interior, which is due to the low content of Si added and the large solid solubility at high temperatures.

Figure 6 shows TEM images of the 0.4 wt.% Si alloy under 950 °C hot compression deformation. It can be seen from Figs. 6(a) and (b) that the precipitate is silicide, and it is rich in Zr and Si. It can be seen from Fig. 6(c) of selected area electron diffraction (SAED) that the matrix is β phase with the BCC structure. The precipitated phase is a hexagonal *S*2-type silicide. Figure 6(d) also shows dislocation aggregation, where *S*2 is present, and DRX grain formation in the microstructure.

Figure 7 shows SEM images of the 0.8 wt.% Si alloy under hot compression at different temperatures. It can be seen from Fig. 7(a) that after hot compression deformation at 850 °C, dot-shaped silicides are distributed in the grain interior. In contrast, the silicides at the grain boundaries are larger at the grain boundaries. Due to the high content of Si added and the presence of the original silicide at the grain boundaries of the as-cast alloy, the volume fraction of silicide at the grain boundaries remains high after the diffusion and redistribution of Si and Zr elements under hot deformation. However, the silicide's continuous distribution at the grain boundary is broken after hot compression deformation compared with the as-cast state. This may be because, on the one hand, a part of the original silicides dissolve at high temperatures; on the other hand, the residual

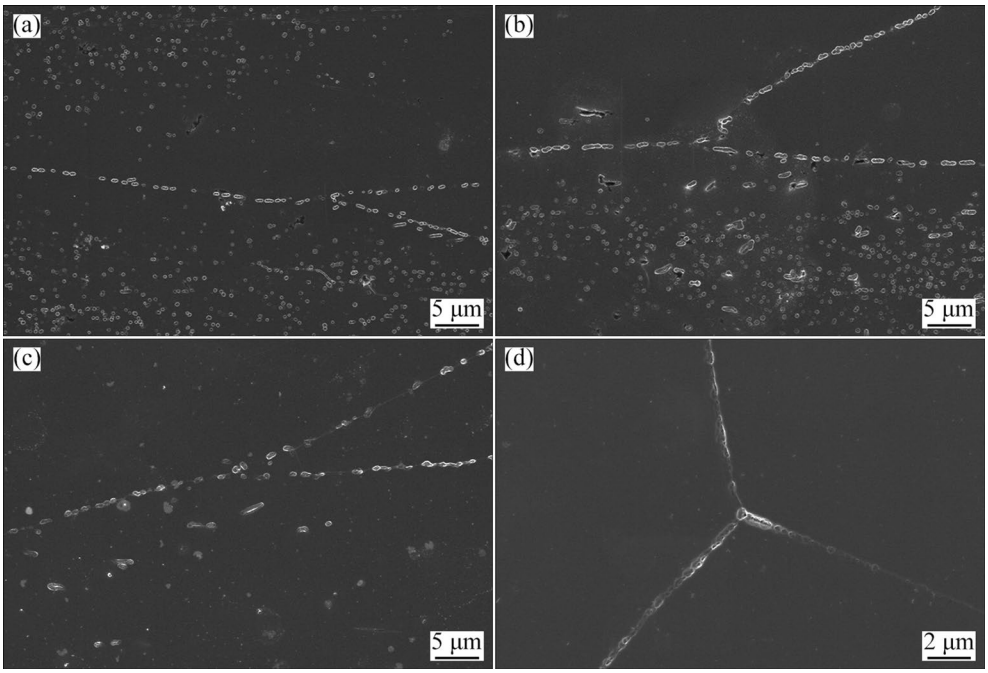

Fig. 5 SEM images of 0.4 wt.% Si alloy under hot compression at different temperatures: (a) 850 °C; (b) 900 °C; (c) 950 °C; (d) 1000 °C

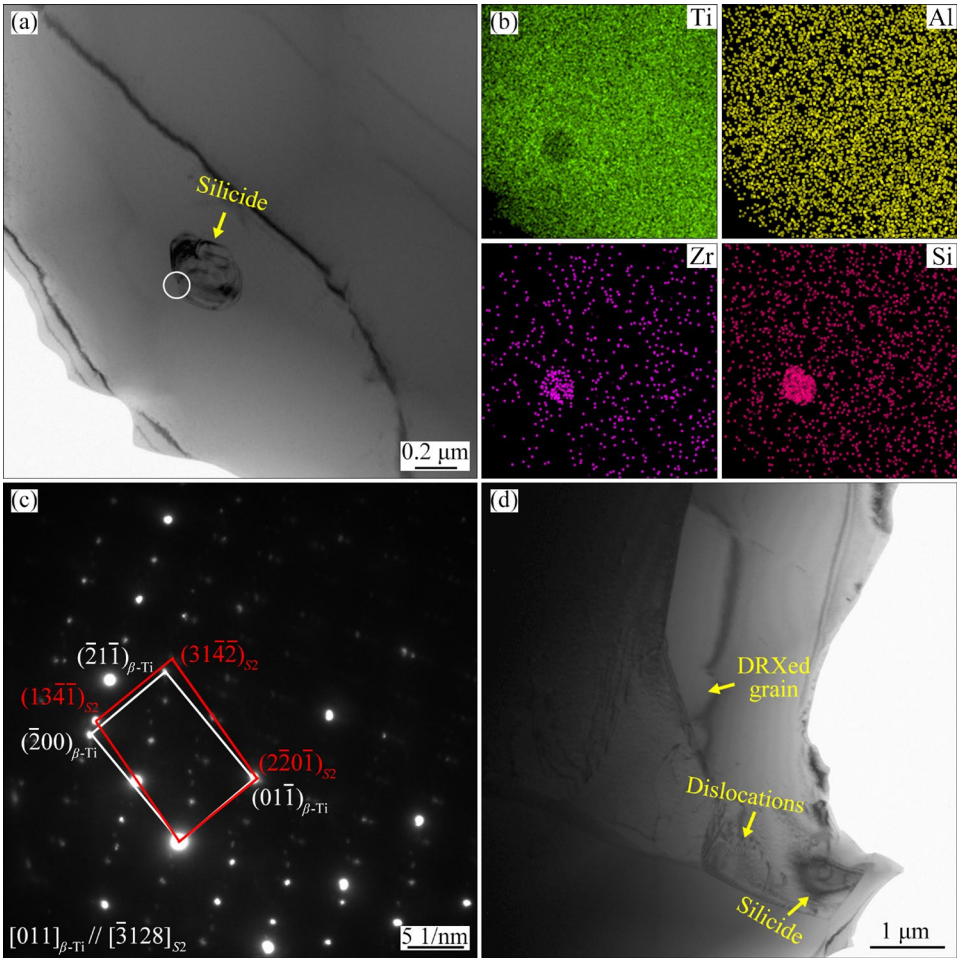

Fig. 6 TEM images of 0.4 wt.% Si alloy under hot compression at 950 °C: (a, d) Bright-field image; (b) EDS mappings in (a); (c) SAED pattern of white circle area in (a)

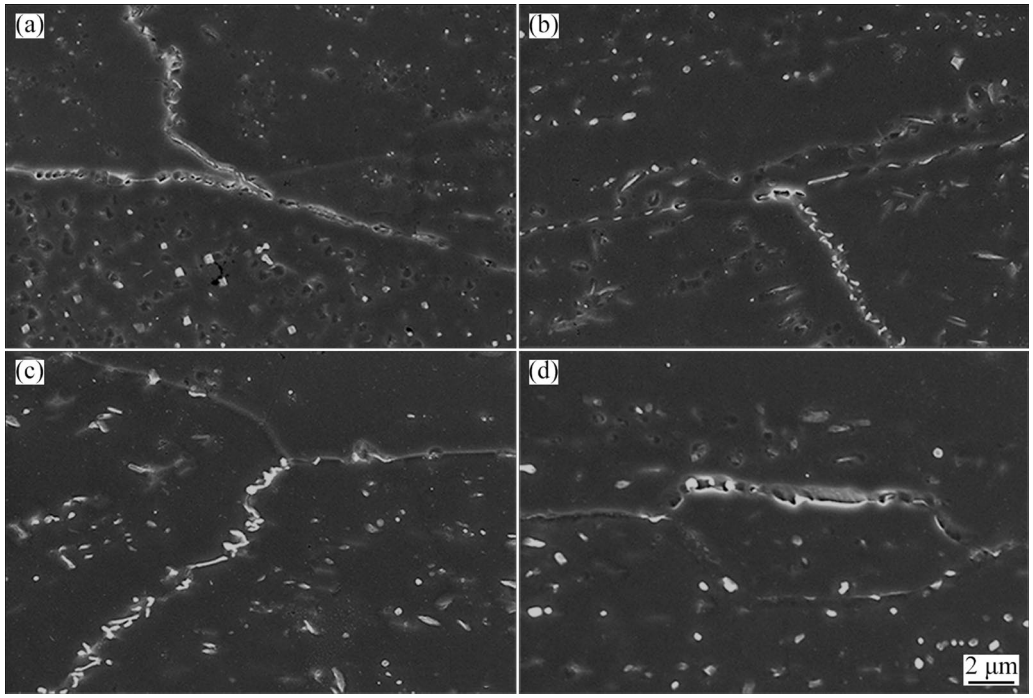

Fig. 7 SEM images of 0.8 wt.% Si alloy under hot compression at different temperatures: (a) 850 °C; (b) 900 °C; (c) 950 °C; (d) 1000 °C

original silicides hinder the dislocation movement in deformation, resulting in stress concentration, and the continuous silicides are broken by force. The silicide morphology is different from the 0.4 wt.% Si alloy in that the length−diameter ratio is increased.

It can be seen from Fig. 8 that the size of intragranular dot-shaped silicides during hot compression deformation of the 0.8 wt.% Si alloy is smaller than that of the 0.4 wt.% Si alloy. This is because silicide precipitation and growth are compete [25]. The 0.8 wt.% Si alloy has a higher Si content, and the presence of the original silicide results in a higher dislocation density the during the deformation. Therefore, silicides have more nucleation sites and constitutional undercooling under hot deformation, which is beneficial to the nucleation of silicides. More diffusion of Si elements is used for nucleation, so more silicides are precipitated, and the size is smaller.

Figure 9 shows the TEM images of 0.8 wt.% Si alloy under 950 °C hot compression deformation. It can be seen from Figs. 9(a) and (b) that some silicides are precipitated and are rich in Zr and Si. It can be seen from Fig. 9(c) that the precipitated phase is a hexagonal *S*2-type silicide. As can be seen from Fig. 9(d), *S*2 is distributed at the grain boundaries and within the grain, and there are high dislocation densities around *S*2, as well as the formation of dislocation walls, which are typical recovery features. Figures 9(e) and (f) show the high-resolution TEM (HRTEM) and corresponding inverse fast Fourier transform (IFFT) images at the interface of *S*2 and matrix β phase. It can be seen that the interface of *S*2 and β phase is not coherent, and due to the larger deformation of β phase compared with *S*2, there are a large number of dislocations and lattice distortions in β phase (Fig. 9(f)).

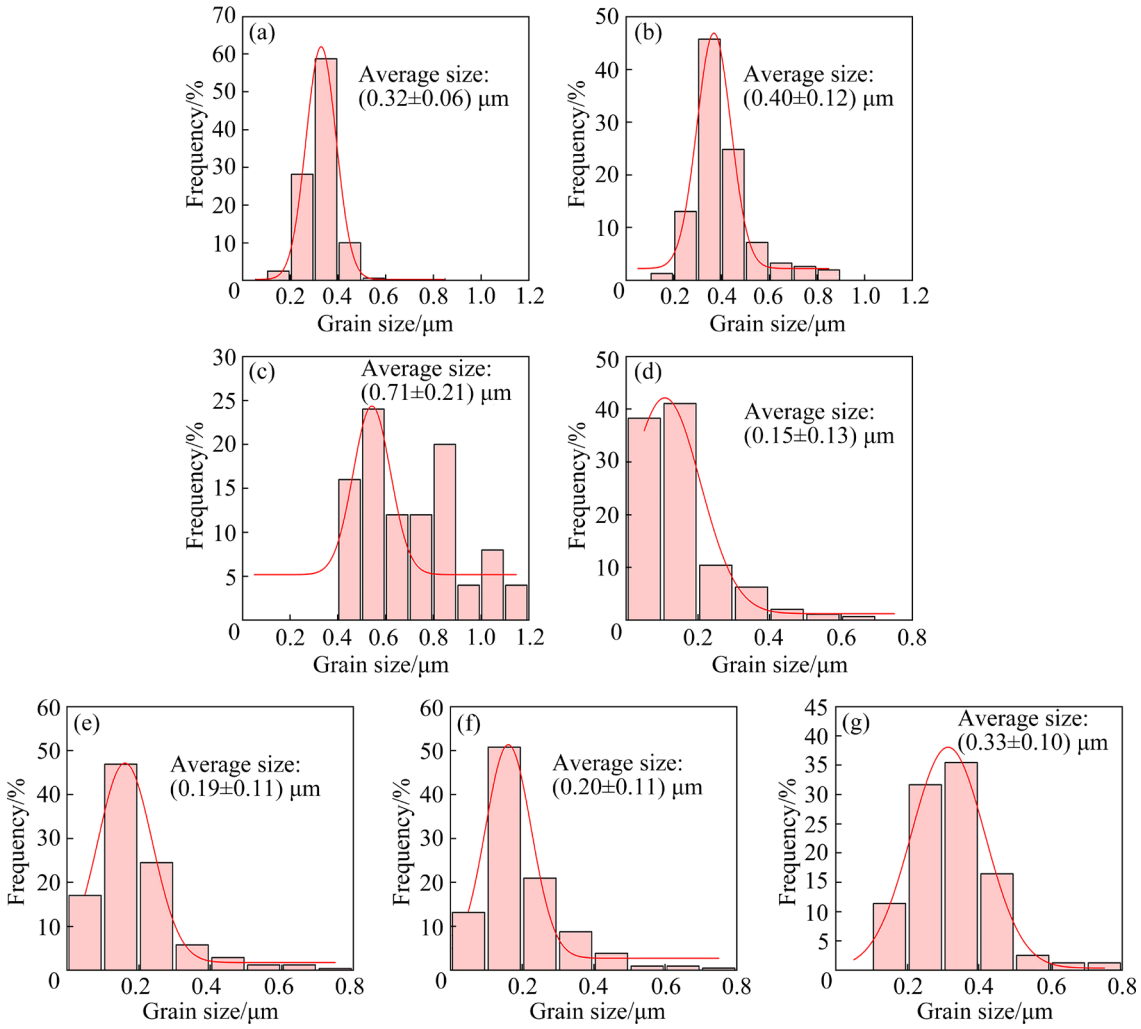

Fig. 8 Size distribution of silicides in grains of 0.4 wt.% Si (a−c) and 0.8 wt.% Si (d−g) alloys after hot compression at different temperatures: (a, d) 850 °C; (b, e) 900 °C; (c, f) 950 °C; (g) 1000 °C

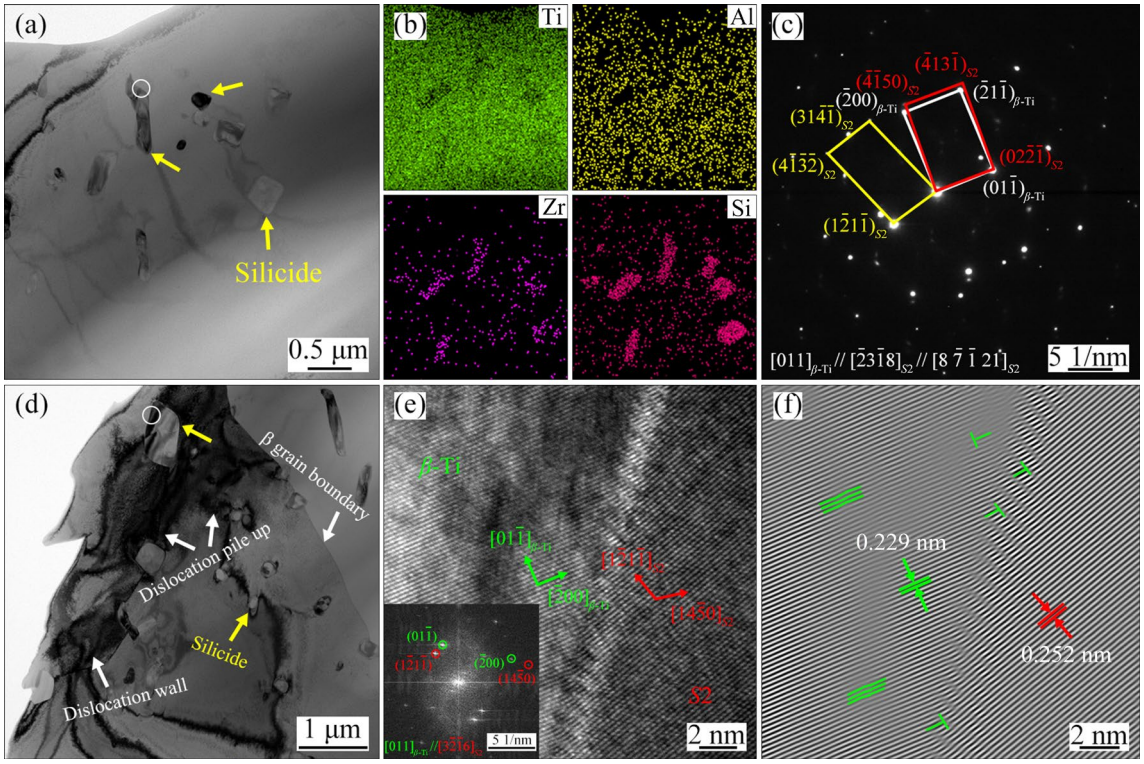

Fig. 9 TEM images of 0.8 wt.% Si alloy under hot compression at 950 °C: (a, d) Bright-field image; (b) EDS mapping of (a); (c) SAED pattern of white circle area in (a); (e, f) Corresponding HRTEM and FFT images of white circle area in (d), respectively

The crystal face spacing of β phase $(01\bar{1})$ is 0.229 nm. The crystal face spacing of $S2$ phase $(1\bar{2}1\bar{1})$ is 0.252 nm.

As can be seen from the EBSD maps of the 0.8 wt.% Si alloy under hot compression in Fig. 10(a), DRV and partial continuous dynamic recrystallization (CDRX) mainly occur under hot deformation at 850 °C. As can be seen from Fig. 10(b), obvious grain boundary serrations are formed under hot compression deformation at 900 °C. When the alloy is hot-compressed at 950 °C, in addition to CDRX, significant discontinuous dynamic recrystallization (DDRX) occurs (Fig. 10(c)). However, at 1000 °C of hot compression, DRX grains appear to grow due to the high temperatures (Fig. 10(d)). It can be seen from kernel average misorientation (KAM) diagrams that the degree of grain accumulation strain decreases with the increase in deformation temperature (Figs. 10(e−h)). As can be seen from Figs. 10(i−l), when the deformation temperature increases, low-angle grain boundaries (LAGBs) transform into high-angle grain boundaries (HAGBs) with DRX, and the number of LAGBs decreases. Because at low temperatures the deformation of the material is dominated by DRV, and the dislocation rearrangement forms subgrains, there are a large number of LAGBs in the microstructure. With the increase in deformation temperature, DRX occurs continuously, and the deformed grains are replaced by recrystallization grains, so the LAGBs decrease and the HAGBs increase.

3.3 Mechanical properties

As can be seen from the Vickers hardness results in Fig. 11(a), with the increase in Si content, the Vickers hardness of the alloy keeps increasing. As the Si content increases from 0 to 1.2 wt.%, Vickers hardness rises from HV 289.50 to HV 333.16 due to the refining of grains, the strengthening of solid solutions, and the strengthening of silicide precipitation [28]. As can be seen from the compressive stress−strain curves in Fig. 11(b), as the Si content increases from 0 to 0.4 wt.%, compressive yield strength ($\sigma_{0.2}$) at room temperature increases from 680 to 832 MPa. As the Si content increases from 0.8 to 1.2 wt.%, the compressive yield strength at room temperature

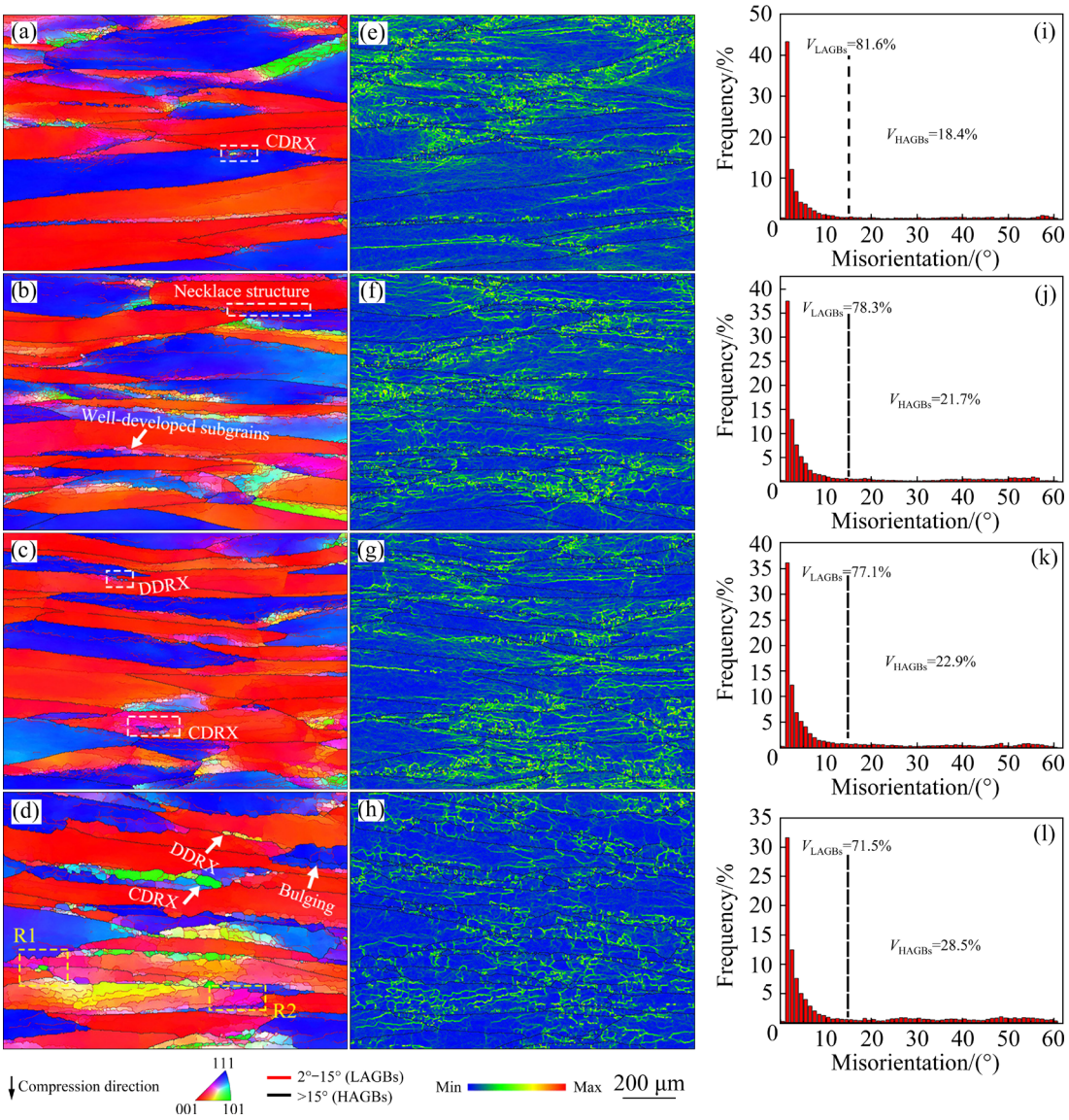

Fig. 10 EBSD maps of 0.8 wt.% Si alloy under hot compression at 850 °C (a, e, i), 900 °C (b, f, j), 950 °C (c, g, k), and 1000 °C (d, h, l): (a−d) IPF maps; (e−h) KAM maps; (i−l) Misorientation distribution (V_{LAGBs} and V_{HAGBs} stand for volume fractions of LAGBs and HAGBs, respectively)

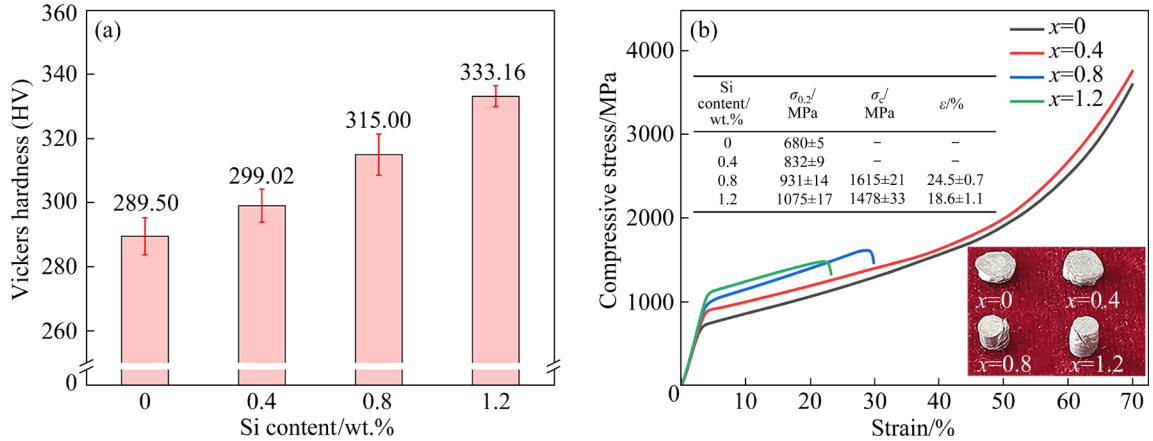

Fig. 11 Vickers hardness (a) and compressive stress−strain curves (b) of as-cast alloys with different Si contents at room temperature

increases from 931 to 1075 MPa, but the plastic strain (ε) to fracture decreases from 24.5% to 18.6% (the strain of the elastic stage was subtracted from the total strain). This is because 0.8 wt.% Si and 1.2 wt.% Si alloys have silicide precipitation at the grain boundary, decreasing alloy plasticity and specimen fracture during room-temperature compression. The existence of the coarse and continuous silicides at the grain boundary makes the moving dislocation accumulate in the grain boundary. It is easy to generate micro-cracks at the grain boundary, and micro-cracks expand rapidly along the grain boundary, resulting in the fracture of the sample [32].

4 Discussion

4.1 Grain refinement and silicide precipitation behavior

According to the experimental results in Fig. 2, the grain size of the as-cast alloy is refined after Si is added, and the grain size decreases with the increase in Si content. It is generally believed that after adding alloying elements, the effect of grain refinement can be achieved through two aspects: one is that there is a potent nucleus in the microstructure to assist nucleation; the other is that the solute atoms cause the constitutional undercooling [20]. According to the Ti−Si binary phase diagram [33,34], the maximum solid solubility of Si in β-Ti is 3 wt.%, and the maximum solid solubility in α-Ti is 0.45 wt.%. In this study, the maximum content of Si was 1.2 wt.%. During the solidification process, silicides do not form before forming the β phase. LIAN et al [25] found by quenching at 1220 °C that silicides were all dissolved. This indicated that silicides did not exist at a high temperature, and silicides were formed during the cooling process of the alloy after solidification, so the refined grains lay in the second aspect, that is, the constitutional undercooling of Si. The partition coefficient of Si in titanium alloy is 0.333. Si is excluded from the front of the liquid/solid interface during the initial solidification process, which leads to solute aggregation and constitutional undercooling, making the liquid/solid interface unstable [29,35]. This increases the driving force of grain nucleation in the melt at the front of the interface, which promotes the nucleation of β grains and refines grains.

This effect of Si on grain refinement by causing constitutional undercooling is also known as the growth-restriction theory; that is, solute aggregation promotes melt nucleation in the undercooled region while limiting the growth of grains that have already been nucleated [36]. For the binary phase diagram, the undercooling effect caused by solute atoms can be evaluated by the growth-restricting factor Q, which is calculated as follows [37]:

$$Q=m(k-1)C_0 \quad (1)$$

where m is the slope of the liquidus, k is the solute partition coefficient ($k=C_S/C_L$, where C_S and C_L denote the solute concentrations at both fronts of the solid/liquid interface in the equilibrium state, respectively), and C_0 is the initial solute concentration. For multi-component alloys, GREER et al [38] and TAMIRISAKANDALA et al [36] showed that the growth-restriction effect of multi-component alloys is equal to the superposition of the growth-restriction effect of each solute. Table 1 lists the growth-restricting factors for different solutes calculated using the binary phase diagram [20,39]. Si exhibits a higher growth-restriction factor than Fe. The larger the growth-restricting factor, the faster the undercooling development and the quicker the nucleation at the interface.

Table 1 Related parameters of growth-restricting factors

Element	m	k	$m(k-1)$
Al	−1.7	→1	→0
V	−2	→1	→0
Zr	−2.3	→1	→0
Cr	−8.1	0.65	2.8
Mo	6.5	2	6.5
Si	−28	0.333	18.7
Fe	−18	0.38	11.1
B	−65	→0	65

A model [40,41] was developed for predicting grain size change in the Al−Mg system, which included the influence of solutes and potent nuclei. EASTON and STJOHN [41] used the model to explain the experimental data and showed the relationship between the grain size and growth-restricting factor Q. The equation is as follows:

$$d=a+b/Q \quad (2)$$

where d is the grain size, a is the constant related to the number of activated nucleant particles ($a=(\rho \cdot f)^{-1/3}$, where ρ is the density of the nucleant particle, and f is the faction of the activated nucleant particle), and b is a constant related to the potency of the nuclei ($b=b_1\Delta T_n$, where b_1 is the constant, and ΔT_n is the undercooling necessary to stimulate nucleation). Figure 12 shows the relationship between the grain size and $1/Q$ in this study; the linear fitting is carried out, and the data are in good agreement. As the addition of Si increased, the growth-restricting factor Q increased, and the grain size d of β grain decreased.

Figure 13 shows the precipitation mechanism of silicide during the solidification process. During solidification, the liquid phase transforms into the solid phase, and the β phase is first formed. In addition, Si has a low partition coefficient in titanium alloys, Si enrichment at the liquid−solid interface in the initial solidification stage, and a high defect density at the grain boundary of the solid phase, so Si element segregation is easy to occur. Then, in the later cooling process, the solid solubility of Si decreases with the decrease in temperature, and the silicide is precipitated in the Si-enriched area. According to the experimental results in Fig. 2, when 0.4 wt.% Si is added, there is no silicide precipitation in the as-cast alloy, whereas when 0.8 wt.% Si and 1.2 wt.% Si are added to the as-cast alloy, silicide precipitation is mainly distributed at the grain boundary, which is continuous and coarse.

Many factors promote the precipitation of silicide. The neutral element Zr, which has a large solid solubility in pure titanium and has a similar size and valence state to Ti atoms, can freely replace Ti. Adding the Zr element can reduce the solid solubility of the Si element in the matrix, reduce the nucleation activation energy of silicide, and promote silicide precipitation [19,42]. XRD results in Fig. 1 indicate that adding Si will cause lattice distortion and β-Ti peak shift, and certain

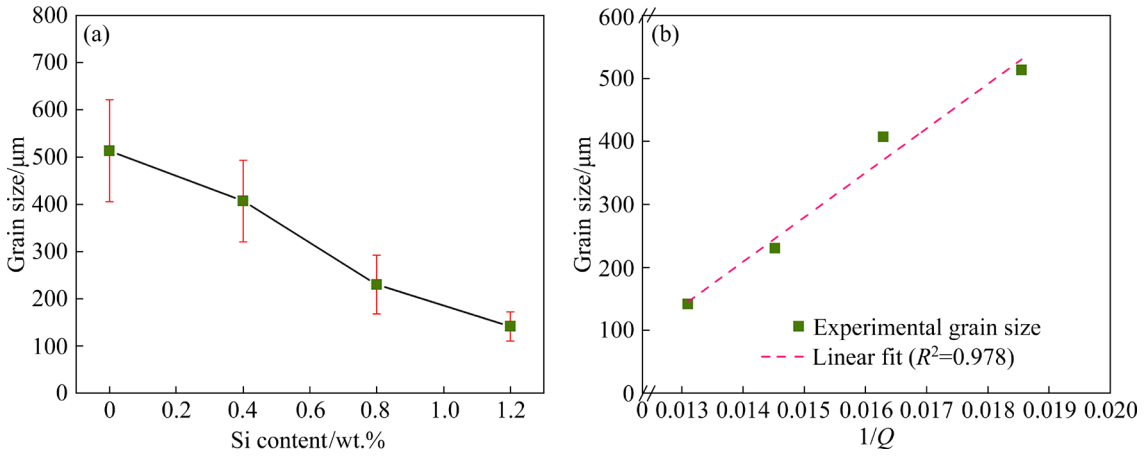

Fig. 12 Grain size of as-cast alloys with different Si contents (a) and change of grain size of as-cast alloys with $1/Q$ (b)

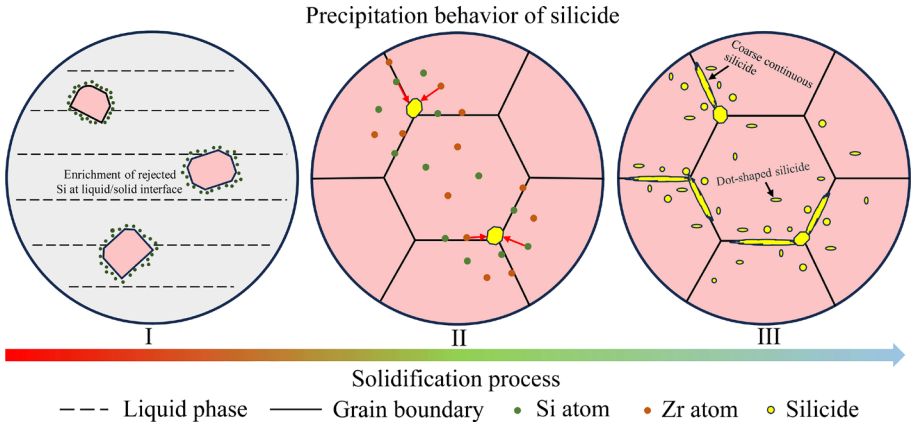

Fig. 13 Schematic diagram of silicide precipitation mechanism during solidification process

distortion energy will be stored in the matrix, providing favorable conditions for silicide precipitation [21]. There are more defects at the grain boundary than in the grain, and the energy of the solute atom at the grain boundary is lower than that in the grain, so the solute atom is easy to diffuse and cause segregation at the grain boundary. The grain boundary storage energy is high, reducing the nucleation power of the precipitated phase and promoting silicide precipitation at the grain boundary.

4.2 Recrystallization behavior and dynamic precipitation of silicide during hot deformation

Figure 14 shows the local EBSD maps of the as-cast alloys with 0.8 wt.% Si under hot compression deformation at 1000 °C. Figures 14(a) and (b) are the magnified maps of Region R1 in Fig. 10(d). It can be seen that the HAGBs show serration shapes with raised segments and DRX nucleation, which are typical of DDRX. The yellow arrow in Fig. 14(b) shows the nucleation of DDRX at the HAGBs. Figure 14(d) shows the magnified image of Region R2 in Fig. 10(d), which reveals the formation of a large number of subgrains in the deformed grains. Figure 14(e) shows the correlated misorientation from *C* to *D* in Fig. 14(d), and it can be seen that the misorientation from *C* to *D* continues to increase. In contrast, the misorientation of adjacent subgrains is relatively close. It can also be seen from Figs. 14(f) and (g) that there are close grain orientations between adjacent subgrains, while the grain orientations change continuously along the *CD* direction. This is typical of CDRX, and recrystallization is brought about by the rotation and growth of subgrains [43]. The DDRX mechanisms associated with HAGBs migration and the CDRX mechanisms associated with subgrain rotation [44] are depicted in the diagram in Fig. 15.

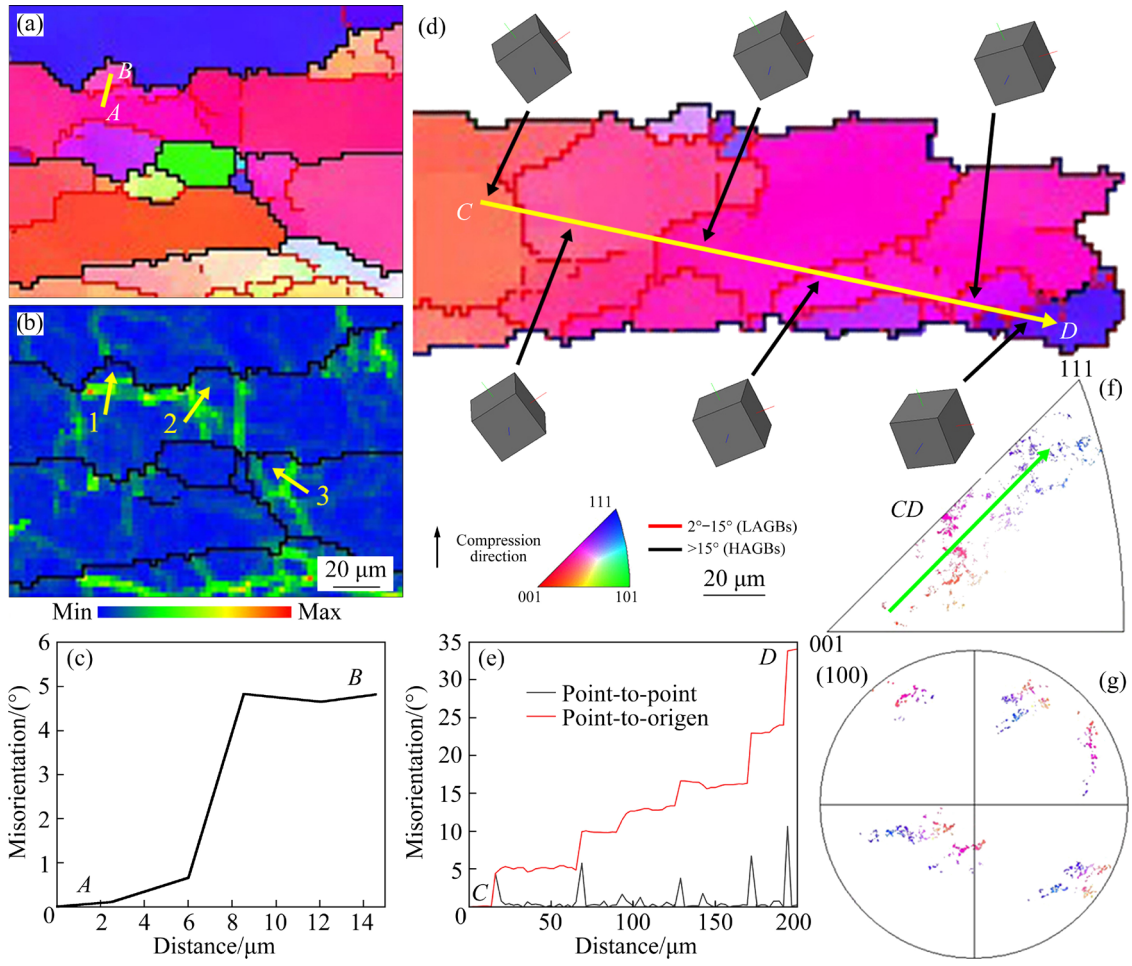

Fig. 14 EBSD maps of as-cast alloy with 0.8 wt.% Si under hot compression at 1000 °C: (a) Magnified IPF map of Region R1 in Fig. 10(d); (b) Magnified KAM map of Region R1 in Fig. 10(d); (c) Correlated misorientation from *A* to *B* as indicated in (a); (d) Magnified IPF map of Region R2 in Fig. 10(d); (e) Correlated misorientation from *C* to *D* as indicated in (d); (f, g) Corresponding IPF and PF maps of (d), respectively

The hot deformation process can promote the precipitation of silicides. LIAN et al [25] found that silicides were diffusely distributed in the matrix of α-titanium alloy after isothermal multidirectional forging, and the volume fraction of silicides increased as the forging temperature decreased. After hot compression of the 0.8 wt.% Si alloy, the discontinuous distribution of silicides is obtained at the grain boundaries, and more dot-shaped silicides are precipitated in the grain interiors (Fig. 7). In hot deformation, the original continuous and coarse silicides at the as-cast alloy grain boundary are broken and dissolved. Zr and Si elements redissolve into the matrix under high temperature and thermal stress, diffusing from the grain boundary to the grain interior depending on the dislocation and nucleating again at the defects, such as the grain boundary and dislocation. The dynamic precipitation of silicide under hot deformation improves the size and distribution of silicide.

The precipitation of silicides during hot deformation and its effect on the microstructure are described in the schematic diagram in Fig. 15. The silicide precipitation is inseparable from the diffusion of Zr and Si elements. During the hot deformation process, Zr and Si elements diffuse and redistribute due to the high diffusion coefficient of solute atoms at high temperatures. In addition, the dislocation generated in the deformation process provides nucleation sites for silicide nucleation and promotes silicide precipitation [22−24]. Figure 9(d) shows a high dislocation accumulation around the silicide. The diffusion rate of Si atoms along the dislocation is much higher than that of the bulk diffusion rate, and the low solubility of Si at a low temperature promotes silicide precipitation [23]. In addition, at a high deformation temperature, the silicide has larger growth dynamics, so the preferentially precipitated silicide shows a growing trend, making the size of the precipitated silicide heterogeneous. On the other hand, with a high defect density at the grain boundary, the solute is easy to segregate. With a low nucleation barrier at the grain boundary, silicides are generally preferentially precipitated at the grain boundary, followed by dislocations, so the size of silicides at the grain boundary is larger [24]. In addition, the recrystallized grain size in the silicide aggregation region is smaller than that in the silicide barren region because of the silicide pinning effect.

4.3 Strengthening mechanisms

According to the experimental results in Fig. 11, the compressive strength of as-cast Ti−4Al−7Mo−4V−3Cr−3Zr−xSi alloys is significantly improved after Si is added. Some of the Si added to the alloy is solute atoms in a solid solution in the matrix, and there is also an interaction between solute atoms and dislocation, which has a solid solution strengthening effect. In addition, due to the growth-restricting effect of Si, the β grain is continuously refined. Grain refinement increases the applied force required to activate adjacent grain dislocation sources. The strengthening effect caused by grain refinement can be described using the Hall−Petch equation [45]:

$$\Delta\sigma_{HP}=k_y(d_y^{-1/2}-d_0^{-1/2}) \quad (3)$$

where k_y denotes the constant of grain boundary effect on strength, d_0 and d_y are the grain sizes of

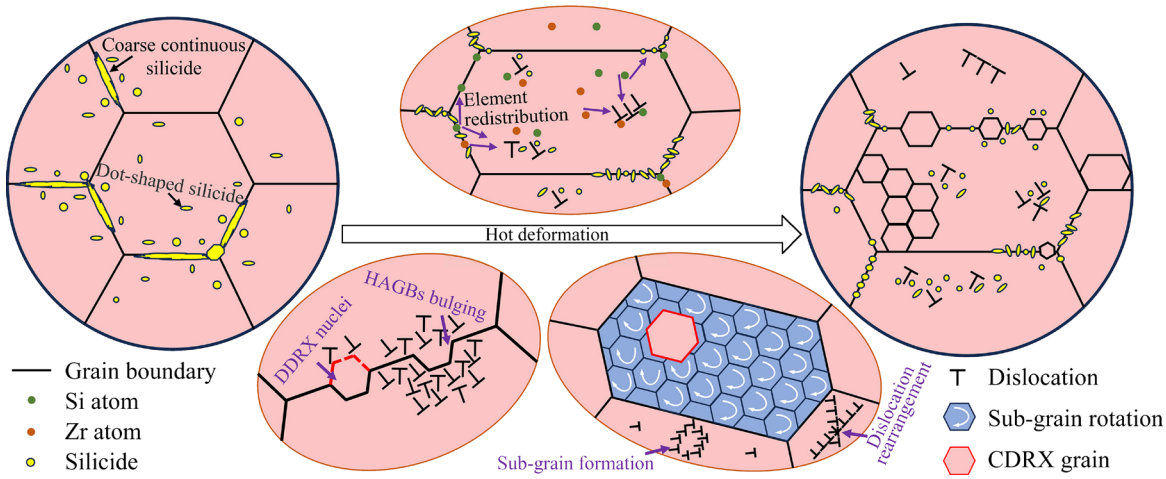

Fig. 15 Schematic diagram of microstructure evolution during hot compression deformation

the as-cast Ti−4Al−7Mo−4V−3Cr−3Zr alloy before and after adding Si.

Due to the high strength and hardness of silicide, the presence of silicide is a strengthening phase of the alloy. According to the TEM characterization in Fig. 9(e), it is found that the interface between silicide and matrix is non-coherent, and silicide particles will hinder the cutting of dislocation in the deformation process, thus hindering the dislocation movement. The 0.8 wt.% Si and 1.2 wt.% Si alloys precipitate dot-shaped silicides in the grain interior, which can impair the dislocation movement and provide a strengthening effect. This strengthening effect can be described using the Ashbye−Orowan equation [46]:

$$\Delta\sigma_{\text{Orowan}}=\frac{0.13G_{\text{m}}b}{\lambda}\cdot\ln\frac{r}{b} \tag{4}$$

where G_{m} and b denote the shear modulus and magnitude of Burgers vector of the matrix, respectively, and r is the radius of the precipitated silicides. The spacing λ of the precipitated silicide can be expressed as

$$\lambda\approx 2r[(2V_{\text{p}})^{-1/3}-1] \tag{5}$$

where V_{p} is the volume fraction of the precipitated silicides.

The strengthening effect at room temperature results from the superposition of various strengthening mechanisms, and the silicide also significantly affects the mechanical properties at high temperatures. According to the experimental results in Fig. 3, 0.8 wt.% Si alloy has a higher peak stress than 0.4 wt.% Si alloy at the same deformation temperature. In high-temperature deformations, the dot-shaped silicide in the grain interior can hinder the dislocation movement, resulting in dislocation accumulation and improved strength. The TEM results in Fig. 9(d) show a large amount of dislocation accumulation around silicides. In addition, silicide at the grain boundary will strengthen the grain boundary and have a strengthening effect.

5 Conclusions

(1) The β grains of the Ti−4Al−7Mo−4V−3Cr−3Zr−xSi (x=0, 0.4, 0.8, 1.2, wt.%) as-cast alloy were continuously refined with the addition of Si, which was attributed to the growth-restricting factor of Si. Coarse and continuous silicides were precipitated at the grain boundaries when the Si content was 0.8 wt.% and 1.2 wt.%, respectively. Intragranular, fine, dot-shaped silicides were precipitated and distributed heterogeneously.

(2) From 850 to 1000 °C, the amount of silicide precipitated by hot compression decreased, but the size increased. At the same time, the precipitated silicide could inhibit the growth of recrystallized grains.

(3) After the hot compression deformation of as-cast alloys with Si contents of 0.4 wt.% and 0.8 wt.%, alloying elements spread rapidly, and the hot deformation promoted the dynamic precipitation of silicide. The discontinuous distribution of silicides was obtained.

(4) The Vickers hardness and room-temperature compression strength of the Ti−4Al−7Mo−4V−3Cr−3Zr−xSi as-cast alloy increased with the addition of Si, which was attributed to the effects of grain refinement, solid solution strengthening, and silicide precipitation strengthening.

CRediT authorship contribution statement

Peng-kun GUO: Methodology, Formal analysis, Investigation, Data curation, Writing − Original draft; **Chang-jiang ZHANG:** Conceptualization, Formal analysis, Resources, Writing − Review & editing, Supervision, Funding acquisition; **Hong FENG:** Methodology, Resources, Visualization; **Fu-yin HAN:** Conceptualization, Methodology, Formal analysis; **Hang LI:** Formal analysis, Visualization; **Jian-chao HAN:** Methodology, Resources, Funding acquisition; **Fan PENG:** Formal analysis, Resources, Funding acquisition; **Peng CAO:** Conceptualization, Resources.

Declaration of competing interest

The authors declare that they have no known competing financial interests or personal relationships that could have appeared to influence the work reported in this paper.

Acknowledgments

This research was funded by the National Natural Science Foundation of China (Nos. 52371117, 52171122, 52275362), the Central Government Guides the Special Fund Projects of Local Scientific and Technological Development, China (Nos. YDZJSX2021A016, YDZX-

20191400002149), the Key Project of Natural Science Foundation of Ningxia, China (No. 2022AAC02077), and the Natural Science Foundation of Shanxi Province, China (No. 20210302124077).

References

[1] BANERJEE D, WILLIAMS J C. Perspectives on titanium science and technology [J]. Acta Materialia, 2013, 61(3): 844−879.

[2] YANG Zhong-ze, XU Wen-chen, ZHANG Wei-qing, CHEN Yu, SHAN De-bin. Effect of power spinning and heat treatment on microstructure evolution and mechanical properties of duplex low-cost titanium alloy [J]. Journal of Materials Science & Technology, 2023, 136: 121−139.

[3] LUO Xuan, LIU Le-hua, YANG Chao, LU Hai-zhou, MA Hong-wei, WANG Zhi, LI Dong-dong, ZHANG Lai-chang, LI Yuan-yuan. Overcoming the strength-ductility trade-off by tailoring grain-boundary metastable Si-containing phase in β-type titanium alloy [J]. Journal of Materials Science & Technology, 2021, 68: 112−123.

[4] JIANG Shan, HUANG Lu-jun, AN Qi, GAO Xiang, WANG Shu-ai, GENG Lin, ZHANG Rui, SUN Feng-bo, JIAO Yang. Significantly strengthening the $Ti_{70}Nb_{10}Mo_{10}Zr_{10}$ alloy via architecting two-scale silicide reinforcements [J]. Journal of Alloys and Compounds, 2020, 835: 155255.

[5] ZHAO Qin-yang, SUN Qiao-yan, XIN She-wei, CHEN Yong-nan, WU Cong, WANG Huan, XU Jian-wei, WAN Ming-pan, ZENG Wei-dong, ZHAO Yong-qing. High-strength titanium alloys for aerospace engineering applications: A review on melting-forging process [J]. Materials Science and Engineering: A, 2022, 845: 143260.

[6] ZHU Wen-guang, LI Pei, SUN Xun, CHEN Wei, ZHANG Hua-lei, SUN Qiao-yan, LIU Bin, XIAO Lin, SUN Jun. Precipitation response and hardening behaviors of Fe-modified Ti5553 alloy [J]. Transactions of Nonferrous Metals Society of China, 2019, 29(6): 1242−1251.

[7] KANG Li-mei, YANG Chao. A review on high-strength titanium alloys: Microstructure, strengthening, and properties [J]. Advanced Engineering Materials, 2019, 21(8): 1801359.

[8] GUPTA A, KHATIRKAR R, SINGH J. A review of microstructure and texture evolution during plastic deformation and heat treatment of β-Ti alloys [J]. Journal of Alloys and Compounds, 2022, 899: 163242.

[9] ZHANG Chang-jiang, JIANG Xi, LÜ Zhi-dan, FENG Hong, ZHANG Shu-zhi, XU Ying, HAYAT M D, CAO Peng. Effect of duplex aging on microstructure and mechanical properties of near-β titanium alloy processed by isothermal multidirectional forging [J]. Transactions of Nonferrous Metals Society of China, 2022, 32(4): 1159−1168.

[10] MOMENI A, ABBASI S M, SADEGHPOUR S. A comparative study on the hot deformation behavior of Ti−5Al−5Mo−5V−3Cr and newly developed Ti−4Al−7Mo−3V−3Cr alloys [J]. Vacuum, 2019, 161: 410−418.

[11] LÜ Zhi-dan, ZHANG Chang-jiang, DU Zhao-xin, HAN Jian-chao, ZHANG Shu-zhi, YANG Fei, CHEN Yu-yong. Relationship between microstructure and tensile properties on a near-β titanium alloy after multidirectional forging and heat treatment [J]. Rare Metals, 2019, 38(4): 336−342.

[12] TAVARES A M G, RAMOS W S, DE BLAS J C G, LOPES E S N, CARAM R, BATISTA W W, SOUZA S A. Influence of Si addition on the microstructure and mechanical properties of Ti−35Nb alloy for applications in orthopedic implants [J]. Journal of the Mechanical Behavior of Biomedical Materials, 2015, 51: 74−87.

[13] BANIA P J. Beta titanium alloys and their role in the titanium industry [J]. JOM, 1994, 46(7): 16−19.

[14] LI Yi-li, FANG Hong-ze, CHEN Rui-run, SUN Shi-chen, XUE Xiang, GUO Jing-jie. Optimization of (α+β) microstructure and trade-off between strength and toughness: Based on $Mo_{[eq]}$ and d electron theory in β-Ti alloy [J]. Materials & Design, 2023, 231: 112022.

[15] EYLON D, VASSEL A, COMBRES Y, BOYER R R, BANIA P J, SCHUTZ R W. Issues in the development of beta titanium alloys [J]. JOM, 1994, 46(7): 14−15.

[16] SUN Shi-chen, FANG Hong-ze, CHEN Rui-run, LI Yi-li, SU Yan-qing, GUO Jing-jie. Discontinuous yield behavior in titanium alloys caused by activated dislocations during tensile testing at room temperature [J]. Scripta Materialia, 2023, 231: 115461.

[17] LU Jin-wen, GE Peng, ZHAO Yong-qing. Recent development of effect mechanism of alloying elements in titanium alloy design [J]. Rare Metal Materials and Engineering, 2014, 43(4): 775−779.

[18] SALPADORU N H, FLOWER H M. Phase equilibria and transformations in a Ti−Zr−Si system [J]. Metallurgical and Materials Transactions A, 1995, 26(2): 243−257.

[19] FU Bin-guo, WANG Hong-wei, ZOU Chun-ming, WEI Zun-jie. The influence of Zr content on microstructure and precipitation of silicide in as-cast near α titanium alloys [J]. Materials Characterization, 2015, 99: 17−24.

[20] BERMINGHAM M J, MCDONALD S D, DARGUSCH M S, STJOHN D H. Grain-refinement mechanisms in titanium alloys [J]. Journal of Materials Research, 2008, 23(1): 97−104.

[21] SUN Shi-chen, FANG Hong-ze, LI Yi-li, ZHANG Xiao-fu, CHEN Rui-run, GUO Jing-jie. Formation mechanism and effect on the mechanical properties of TiSi phase for Ti−5Al−5Mo−5Cr−3Nb−2Zr alloyed by silicon [J]. Journal of Alloys and Compounds, 2023, 938: 168510.

[22] ZHAO Er-tuan, SUN Shi-chen, ZHANG Yu. Recent advances in silicon containing high temperature titanium alloys [J]. Journal of Materials Research and Technology, 2021, 14: 3029−3042.

[23] SUN Shi-chen, ZHAO Er-tuan, HU Chen, AN Yu-kun, CHEN Wen-zhen. Precipitation behavior of silicide and synergetic strengthening mechanisms in TiB-reinforced high-temperature titanium matrix composites during multi-directional forging [J]. Journal of Alloys and Compounds, 2021, 867: 159051.

[24] LUO Xuan, SONG Tao, WANG Feng, LU Hai-zhou, KANG Li-mei, MA Hong-wei, LI Dong-dong, GEBERT A, YANG Chao. Phase selection-oriented mechanical properties

tailoring for β-type TiNbZrTaSi alloy fabricated by laser powder bed fusion [J]. Advanced Powder Materials, 2023, 2(3): 100118.

[25] LIAN Qi-hao, ZHANG Chang-jiang, FENG Hong, ZHANG Shu-zhi, PENG Fan, CAO Peng. Enhanced mechanical properties of a near-α titanium alloy by tailoring the silicide precipitation behavior through severe plastic deformation [J]. Materials Science and Engineering: A, 2023, 880: 145356.

[26] LIAN Qi-hao, ZHANG Chang-jiang, FENG Hong, YANG Zhen-bo, ZHANG Shu-zhi, HAN Jian-chao, WANG Tao, PENG Fan, CAO Peng. Hot deformation temperature and pre-deformation effect on silicide precipitation behavior of (TiB+Y_2O_3)/near α-Ti matrix composite [J]. Transactions of Nonferrous Metals Society of China, 2023, 33(9): 2660−2671.

[27] LI Chang-min, HUANG Liang, ZHAO Ming-jie, GUO Shi-qi, LI Jian-jun. Hot deformation behavior and mechanism of a new metastable β titanium alloy Ti−6Cr−5Mo−5V−4Al in single phase region [J]. Materials Science and Engineering: A, 2021, 814: 141231.

[28] LUO Xuan, YANG Chao, LI Rui-yan, WANG Hao, LU Hai-zhou, SONG Tao, MA Hong-wei, LI Dong-dong, GEBERT A P, LI Yuan-yuan. Effect of silicon content on the microstructure evolution, mechanical properties, and biocompatibility of β-type TiNbZrTa alloys fabricated by laser powder bed fusion [J]. Biomaterials Advances, 2022, 133: 112625.

[29] BERMINGHAM M J, MCDONALD S D, DARGUSCH M S, STJOHN D H. The mechanism of grain refinement of titanium by silicon [J]. Scripta Materialia, 2008, 58(12): 1050−1053.

[30] LI Chang-min, HUANG Liang, LI Cheng-lin, HUI Song-xiao, YU Yang, ZHAO Ming-jie, GUO Shi-qi, LI Jian-jun. Research progress on hot deformation behavior of high-strength β titanium alloy: flow behavior and constitutive model [J]. Rare Metals, 2022, 41(5): 1434−1455.

[31] SHI Shuang-xi, LIU Xiu-sheng, ZHANG Xiao-yong, ZHOU Ke-chao. Comparison of flow behaviors of near beta Ti-55511 alloy during hot compression based on SCA and BPANN models [J]. Transactions of Nonferrous Metals Society of China, 2021, 31(6): 1665−1679.

[32] ZHAO Ding, FAN Jiang-kun, ZHANG Zhi-xin, WANG Jing, WANG Qing-jiang, CHEN Zhi-yong, TANG Bin, KOU Hong-chao, LI Jin-shan. Influence of α+β solution treatments on Ti65 ultrathin sheets: Silicide precipitation, mechanical behaviour and novel $\{10\bar{1}1\}$ twinning system [J]. Transactions of Nonferrous Metals Society of China, 2023, 33(4): 1098−1113.

[33] SEIFERT H J, LUKAS H L, PETZOW G. Thermodynamic optimization of the Ti−Si system [J]. Zeitschrift für Metallkunde, 1996, 87(1): 2−13.

[34] FIORE M, BENEDUCE NETO F, de FARIAS AZEVEDO C R. Assessment of the Ti-rich corner of the Ti−Si phase diagram: The recent dispute about the eutectoid reaction [J]. Materials Research, 2016, 19(4): 942−953.

[35] JANG J H, LEE D G. Effects of silicon and heat-treatment on microstructure and mechanical properties of biomedical Ti−39Nb−6Zr alloy [J]. Metals, 2021, 11(2): 268.

[36] TAMIRISAKANDALA S, BHAT R B, TILEY J S, MIRACLE D B. Grain refinement of cast titanium alloys via trace boron addition [J]. Scripta Materialia, 2005, 53(12): 1421−1426.

[37] MAXWELL I, HELLAWELL A. A simple model for grain refinement during solidification [J]. Acta Metallurgica, 1975, 23(2): 229−237.

[38] GREER A L, COOPER P S, MEREDITH M W, SCHNEIDER W, SCHUMACHER P, SPITTLE J A, TRONCHE A. Grain refinement of aluminium alloys by inoculation [J]. Advanced Engineering Materials, 2003, 5(1/2): 81−91.

[39] BERMINGHAM M J, MCDONALD S D, STJOHN D H, DARGUSCH M S. Segregation and grain refinement in cast titanium alloys [J]. Journal of Materials Research, 2009, 24(4): 1529−1535.

[40] STJOHN D H, QIAN M, EASTON M A, CAO P, HILDEBRAND Z. Grain refinement of magnesium alloys [J]. Metallurgical and Materials Transactions A, 2005, 36(7): 1669−1679.

[41] EASTON M, STJOHN D. An analysis of the relationship between grain size, solute content, and the potency and number density of nucleant particles [J]. Metallurgical and Materials Transactions A, 2005, 36(7): 1911−1920.

[42] GUO Rui, LIU Bin, XU Rong-jun, CAO Yuan-kui, QIU Jing-wen, CHEN Feng, YAN Zhi-qiao, LIU Yong. Microstructure and mechanical properties of powder metallurgy high temperature titanium alloy with high Si content [J]. Materials Science and Engineering: A, 2020, 777: 138993.

[43] LU Tong, DAN Zhen-hua, LI Kai, YI Dan-qing, ZHOU Lian, CHANG Hui. Hot deformation behaviors and dynamic recrystallization mechanism of Ti-35421 alloy in β single field [J]. Transactions of Nonferrous Metals Society of China, 2022, 32(9): 2889−2907.

[44] HUANG Liang, LI Chang-min, LI Cheng-lin, HUI Song-xiao, YU Yang, ZHAO Ming-jie, GUO Shi-qi, LI Jian-jun. Research progress on microstructure evolution and hot processing maps of high strength β titanium alloys during hot deformation [J]. Transactions of Nonferrous Metals Society of China, 2022, 32(12): 3835−3859.

[45] HE Jun-yang, WANG Hui, HUANG Hai-long, XU Xian-dong, CHEN Ming-wei, WU Yuan, LIU Xing-jiang, NIEH Tai-gang, AN Ke, LU Zhao-ping. A precipitation-hardened high-entropy alloy with outstanding tensile properties [J]. Acta Materialia, 2016, 102: 187−196.

[46] ZHANG Z, CHEN D L. Consideration of Orowan strengthening effect in particulate-reinforced metal matrix nanocomposites: A model for predicting their yield strength [J]. Scripta Materialia, 2006, 54(7): 1321−1326.

一种含硅近β钛合金中硅化物的析出行为及其对晶粒细化的影响

郭鹏坤[1]，张长江[1,2,3]，冯 弘[1]，韩富银[1]，李 航[1]，韩建超[3]，彭 凡[2]，曹 鹏[4]

1. 太原理工大学 材料科学与工程学院，太原 030024；
2. 共享装备股份有限公司，银川 750021；
3. 先进金属复合材料成形技术与装备教育部工程研究中心，太原 030024；
4. Department of Chemical and Materials Engineering, University of Auckland, New Zealand

摘 要：研究了添加 Si 对一种新型近β钛合金显微组织和硅化物析出行为的影响。结果表明：在凝固过程中粗大、连续的硅化物优先在晶界处析出，铸态合金β晶粒尺寸得到细化。在等温热压缩变形下发生了动态再结晶，且析出的硅化物能抑制再结晶晶粒的长大。热变形过程中的元素重新分布和位错积累促进硅化物的动态析出，从而导致硅化物在晶界处呈不连续分布。这项工作为研究硅化物动态析出对合金显微组织和塑性变形行为的影响提供了深入的见解。

关键词：近β钛合金；热压缩；硅化物；晶粒细化；动态析出

(Edited by Wei-ping CHEN)